International Journal of Fatigue 151 (2021) 106350

Contents lists available at ScienceDirect

International Journal of Fatigue

journal homepage: www.elsevier.com/locate/ijfatigue

Digital image correlation for continuous mapping of fatigue crack initiation sites on corroded surface from offshore mooring chain

Paul Qvale [a,*], Ershad P. Zarandi [a], Sigmund K. Ås [b], Bjørn H. Skallerud [a]

[a] Department of Structural Engineering, Norwegian University of Science and Technology (NTNU), NO-7491 Trondheim, Norway
[b] Department of Marine Technology, NTNU, NO-7491 Trondheim, Norway

ARTICLE INFO

Keywords:
Fatigue initiation
Digital image correlation
Finite elements
Corrosion fatigue
Offshore engineering

ABSTRACT

The full-field digital image correlation (DIC) technique was used to identify crack initiation and early crack growth on irregular, corroded surfaces from offshore mooring chain. Finite element analysis was paired with the DIC measurements, which made it possible to correlate initiation events with local stress concentrations due to corrosion pits. An initiation S-N curve was established based on this correlation. It included 14 crack initiation events from 4 specimens, in addition to statistical treatment of regions where no initiation occurred. The first cracks initiated at 13–24% of the total lifetimes of the specimens.

1. Introduction

Mooring chains are an integral part of floating structures for offshore energy production. In service, they have a limited lifetime, and corrosion fatigue is an important degradation mechanism. General corrosion reduces the cross section areas, and pitting corrosion raises the cyclic stress ranges locally[1,2]. Replacing the mooring chains on a production unit represents a significant cost for the operator. Thus, the industry needs more accurate lifetime estimates, allowing for more timely replacement of the chains. This could improve safety and reduce costs and environmental impact.

A number of chain segments have been fatigue tested in artificial sea water during the past decades[3,4]. Although full-scale corrosion fatigue tests give valuable benchmark data, it is still a challenge to use these results for in-service lifetime prediction. In order for the tests to finish within a reasonable time, the applied cyclic loads and load frequencies have been higher than those experienced by the chains in service. Since corrosion is a time dependent process, effects of the corrosive environment on fatigue is decreased when tests are accelerated. Considering this effect alone, full-scale laboratory data would give non-conservative predictions when applied to in-service chains. Test temperature also affects free corrosion crack growth, and in this case the laboratory tests conducted at room temperature would be detrimental to fatigue life, i.e. conservative compared to the in-service temperatures experienced during the winter months in the North and Norwegian Sea [5]. There are several other uncertainties that exacerbate this fundamental problem of using corrosion fatigue lab data in the real world, such as the use of constant amplitude data for in-service spectrum loading, choice of damage accumulation methods, mean stress corrections, and others[6–8]. The various approaches to account for these effects in lifetime prediction typically distinguish between initiation mechanisms and crack growth mechanisms. Detailed studies have been made on the initiation of cracks from pits[9–15] that have provided valuable insights into growth of small cracks from corrosion pits. Whereas these efforts were aimed at single artificially created pits, the current study is aimed at detecting initiation events within a larger area of corroded surfaces, either on full-scale chain links or on small-scale specimens.

Digital image correlation (DIC) is a full-field, optical monitoring technique that can be used to track displacements on a surface from a series of sequentially captured images[16]. The method has been used to gain valuable insight into fatigue crack behavior on a macro (continuum) scale [17,18] and micro scale [19]. Crack initiation from the mouth of an artificial corrosion pit in a smooth specimen has been monitored[10], and in a fatigue test a specimen with an electropolished surface, multiple microcrack initiation sites were revealed using DIC [20]. To the authors' knowledge, there has been no attempt to monitor fatigue crack initiation on a surface with general corrosion from service, like that of an offshore mooring chain.

The motivation for the current work is to promote detection of crack initiation in both small-scale and full-scale testing. Initiation life in this paper is defined, using the recorded surface displacements, as the

* Corresponding author.
E-mail address: paul.qvale@ntnu.no (P. Qvale).

https://doi.org/10.1016/j.ijfatigue.2021.106350
Received 29 March 2021; Received in revised form 12 May 2021; Accepted 24 May 2021
Available online 28 May 2021

number of cycles until a crack of a certain size can be detected. An initiation event is thus not related to the micromechanical process of forming a crack from persistent slip bands[6]. Rectangular bar specimens were extracted from mooring chain links retrieved from service, while keeping one face as-corroded. The specimens were subjected to cyclic loading in a three-point bending test setup in an air environment. DIC was used to measure displacement histories for a grid of points on the corroded surface. Early signs of crack initiation across the corroded specimen surface were captured by applying an initiation criterion to the displacement histories of the points in the grid, to determine the fatigue lifetime spent on initiation and growth, respectively. Finite element analysis (FEA) was performed on scanned specimen geometries to calculate the stresses at initiation sites. The database of initiation events was used to establish an initiation *S-N* curve for a surface element of a corroded mooring chain link.

2. Methodology

2.1. Experimental details

2.1.1. Specimen preparation

Four fatigue test specimens were cut from the non-welded straight section of two connected Ø114 mm mooring chain links, see Fig. 1. The links were made from R4 grade high-strength steel. Monotonic and cyclic yield strengths of 843 MPa and 630 MPa, respectively, have been measured on similar links[21]. The links had been retrieved from chains that had been in service on a floating production storage and offloading (FPSO) unit in the Norwegian Sea for 15 years. The two links had been exposed to identical service loads and environment. The specimens were cut from the chain links using electrical discharge machining (EDM), and then milled to their final dimensions, as shown in Fig. 2. The coordinate system in the figure will be used as a reference throughout this work. It can be assumed that residual stresses from production of the chains[22,23] were relieved from the specimen material when the specimens were extracted.

To remove corrosion products and expose the bare metal surface for optical fatigue monitoring, the corroded specimens were degreased and cleaned in a hydrochloric acid solution according to ASTM G1 - 03 (2017) e1, procedure C.3.5[24]. Degreasing and cleaning was done in an ultrasonic acetone bath. Thereafter, the specimens were lightly brushed to remove remaining corrosion products. After the treatment, some

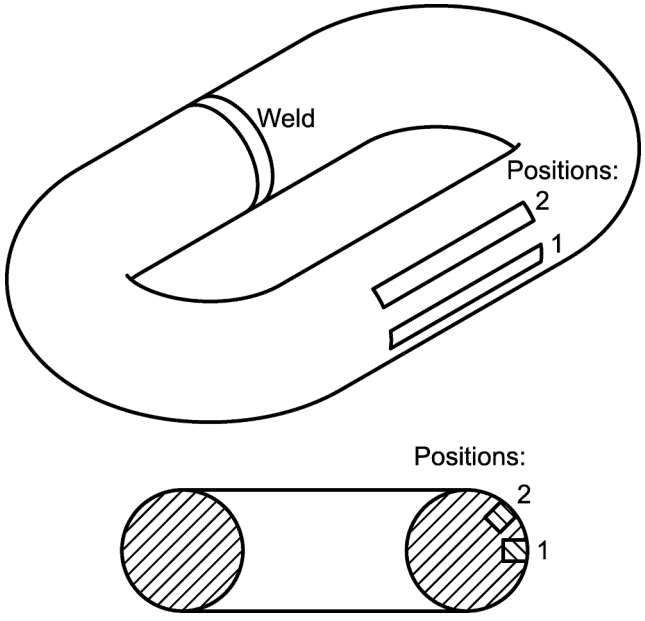

Fig. 1. Extraction locations of specimens in a chain link.

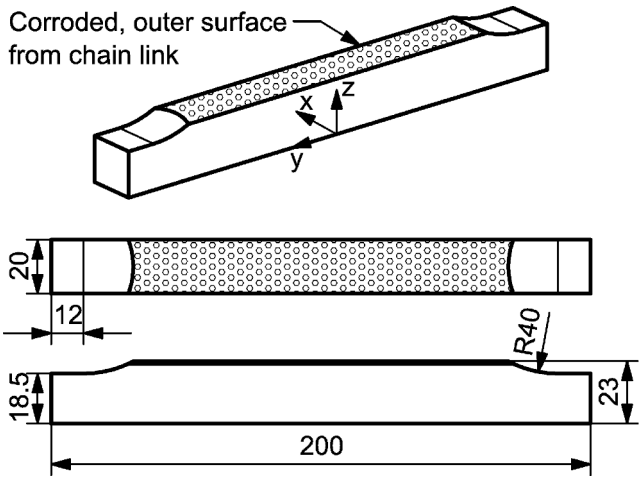

Fig. 2. Dimensions of specimens in millimeters. Reference coordinate system is shown.

corrosion products still remained in the deepest pits. However, since the metal surface everywhere else on the corroded surfaces had been successfully exposed, the result was considered satisfactory. Ideally, no corrosion product should have been left on the specimens. Nevertheless, more aggressive cleaning procedures were not attempted, to avoid risk of damaging the surfaces. Fig. 3 shows the corroded surfaces of the specimens after cleaning.

2.1.2. Fatigue test setup

The specimens were loaded cyclically in a three-point bending setup as shown in Fig. 4. The specimens had been extracted from the straight part of chain links, to provide a corroded surface with a convenient shape for fatigue testing. However, the moment load induced by a three-point bending setup resembles more closely that found in the crown of a loaded chain link, where the majority of failures in recent full-scale tests have been found to occur[25]. The load levels that were used are shown in Table 1. The loads correspond to a nominal stress ratio (of minimum to maximum stress) of $R = 0.2$. The loads were applied using a triangular wave shape and a frequency of 3 Hz. Loading was applied using an Instron 8800 250 kN test system and an A10025E cylinder with a stroke of 250 mm. An Instron 250 kN load cell was used. Load cell calibration performed 2 years before testing was executed showed 0.2% deviation at 25 kN tension load.

2.1.3. Monitoring by DIC

A random, monochrome surface pattern was needed to provide surface references for the DIC monitoring. The corroded surfaces of the specimens were sprayed with a thin coat of white paint. Thereafter, a light dust of black paint was applied, leaving the specimens with a fine speckle pattern.

For acquiring images, one 12.3-megapixel Basler acA4112-30um camera with a Sony IMX304 CMOS sensor and a Samyang 100 mm f/2.8 ED UMC Macro lens was mounted on each side of the testing rig in a manner shown for one side in Fig. 5. A two-camera setup was used, to be able to capture displacements on different sides of surface features, and to allow for 3D post-processing of DIC images. Nevertheless, the algorithms developed in this work only made use of 2D displacements. Since a beam in the testing rig prevented the placement of a camera directly below the surface, the cameras had to be placed at a 48°angle to the surface normal. This setup allowed for sufficient depth of field to obtain images that covered the width of a specimen. The photographed mid-sections had lengths of 40–42 mm. The image resolution was 3000 pixels (px) in the *y* direction. A Metz Mecalight LED-480 LED panel was placed 85 mm below the specimen surface to keep the shutter times low. The cameras were triggered at the peak load of every 100th load cycle.

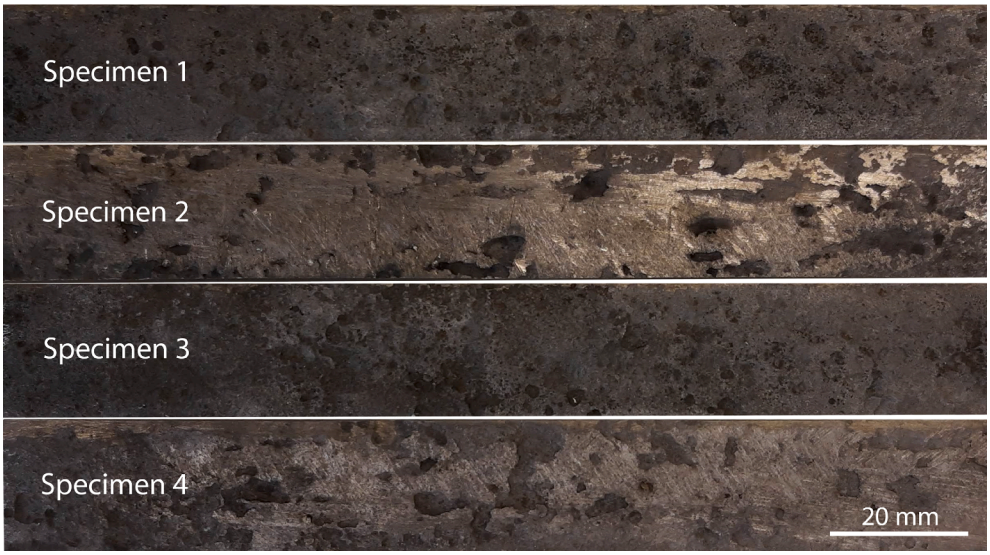

Fig. 3. Cleaned corroded surfaces of the specimens.

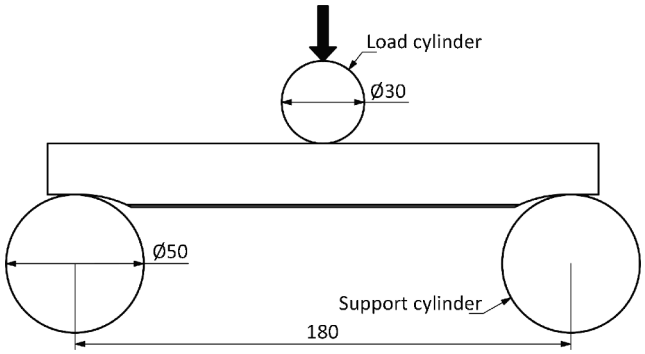

Fig. 4. Three-point bending setup used for fatigue testing.

Camera shutter times were 15–20 ms.

Post-processing of images was carried out in the in-house, finite-element based DIC code eCorr v4.0[26]. A mesh consisting of 15-by-15 px, isoparametric Q4 bilinear quadrilateral elements was created to track the coordinate evolutions on the relevant surface. This corresponds to an element length of 0.2 mm in the y direction and 0.3 mm in x direction of the specimen. Each element had four corner nodes, and consequently, each node was shared between four elements.

In the current work, crack initiation on the surfaces of the fatigue test specimens was detected by imposing a criterion on sub-pixel, inter-node displacement of the DIC mesh as load cycling progressed. The nodal coordinate histories were imported to the numeric computing environment MATLAB, and the following criterion was implemented on the nodal displacements in the y direction of the specimens:

The distance between a node and its neighbor is thought of as a material ligament. A ligament is considered broken, and thus, a crack is defined as initiated, when the ligament length has increased by 0.15 px (2 μm) above its all-time minimum.

Fig. 6 illustrates the criterion. Fig. 7 provides an example of an inter-node displacement history and application of the criterion. To avoid false indications of initiation caused by noise in the DIC measurements, a ten-point moving average of the displacement histories were used. As an additional measure against temporary fluctuations in ligament length, only ligaments eventually reaching 0.90 px (13 μm) of extension were considered real initiation points. The last intersection of the displacement curve with the 0.15 px limit was defined as the initiation time. As will be shown, the criterion produced realistic initiation events and subsequent crack growth with few erroneous indications.

Tilting of the cameras relative to the specimens introduced a small error in the DIC measurements. Since the camera sensor was parallel with the specimen y axis, the error along this axis due to perspective distortion could be readily estimated. With the current camera setup, the distance from the center of the lenses to the specimen surfaces was around 520 mm. Geometric calculations showed that measurements of a displacement in the y direction on the edges of the specimen could differ by $\pm$1.3% compared to measurements made in the x-z midplane. This error was considered negligible for the purpose of using the crack initiation detection criterion.

It should be noted that a more pronounced error can occur regardless of camera angle when cracks start to grow large in a specimen in a bending fatigue setup. As the bending stiffness is reduced, the deflection at maximum load along the loading axis increases cycle by cycle. In relation to the camera sensor, this results in an out-of-plane displacement, which eventually causes a significant error in the inter-node displacement measurements. For reasons described later, the DIC processing in the current work was limited to detection of cracks as long as they remained relatively small. In this domain, the recorded deflection at maximum load at the position of the load roller did not increase more than 0.14 mm for any specimen. Calculations for the current camera angle showed that this resulted in a maximum error of only 2.0% on displacements measured with DIC, which was deemed negligible.

Table 1
Load levels for each specimen and original positions on the chain links. The highest nominal stresses in y direction at the surface of a specimen are also given.

Specimen ID	Link ID	Position on link	Load amplitude/kN	Mean load/kN	Nominal stress amplitude/MPa	Nominal mean stress/MPa
1	1	1	8	12	211	317
2	1	2	10	15	263	395
3	2	1	8	12	211	317
4	2	2	10	15	263	395

Fig. 5. One side of test rig with camera.

2.2. Surface scanning and FEA

For the purpose of stress calculations by FEA, all specimens were surface scanned using a GOM ATOS 5 8MP scanner with a MV170 lens pair, with a measurement volume of 170x130x130 mm. The system is based on fringe projection [27] and optical triangulation for relative positioning of multiple scans. The specimens were placed on a software controlled rotary table, thus multiple scans from different angles could be collected automatically to cover all sides of the surface pits. The size probing error and sphere spacing error have been found to be 6 μm and -4 μm, respectively, according to VDI/VDE 2634–3:2008 test procedures. GOM Inspect 2019 software was used for processing the scans, using the "high detail" setting to retain as much detail from the point cloud as possible. Autofill was applied in GOM Inspect to close holes that appeared in a few deeply recessed or dark areas. Finally, the mesh was smoothed with a surface tolerance of 0.01 mm in order to remove smaller asperities. The resulting surface meshes were regularized in the modelling software ANSYS SpaceClaim by applying its "shrinkwrap" feature. A 0.15 mm element size was used on the surface of the midsection of the specimens. In the FEA software ANSYS Mechanical, solid, quadratic-order tetrahedron meshes were generated, applying a slow transition from the midsection element size to a global element size of 1.5 mm. An example of a meshed specimen is shown in Fig. 8.

A mesh sensitivity analysis was carried out for the midsection element size. For a semi-spherical Ø2 mm pit in the middle of an otherwise smooth specimen surface, 0.15 mm and 0.22 mm size elements provided nearly identical results for stresses in the y direction. A mesh consisting of 0.35 mm elements gave slightly deviating results. Thus, it can be concluded that both a 0.15 mm and 0.22 mm element mesh are of adequate resolution for accurate stress calculation for a pitted surface.

For FEA of the specimens, loading was applied as concentrated line loads and displacements at the position of the rollers in the testing rig. As will be seen, stress amplitudes remained below the cyclic yield strength across all specimen surfaces. Thus, a monotonic material model for R4

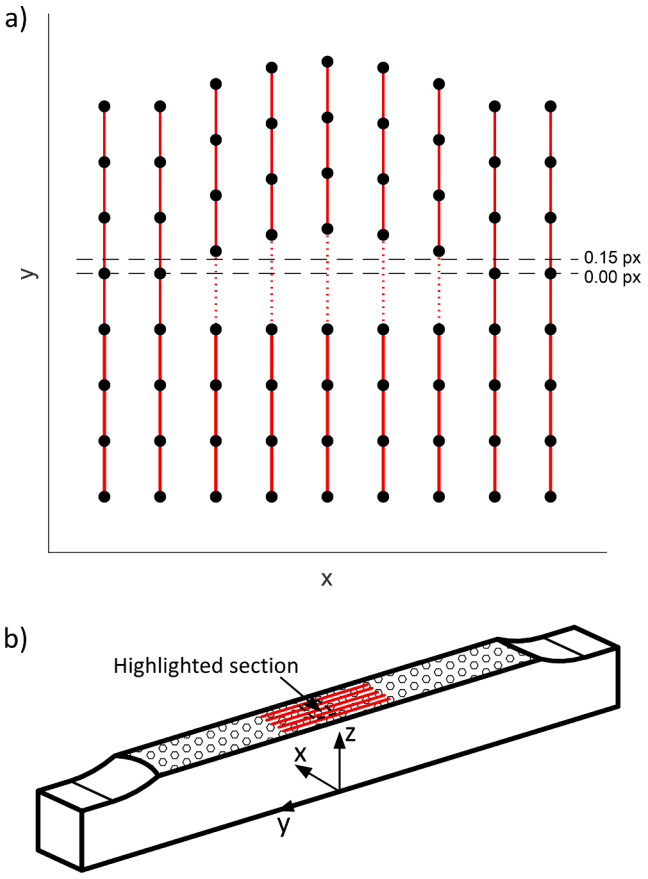

Fig. 6. Schematic illustration of a) crack initiation criterion on DIC results on b) the midsection of a specimen. The black dots in a) represent DIC mesh nodes. Surface material ligament (red) was considered broken if inter-node displacement exceeded 0.15 px, corresponding to a displacement of 2 μm.

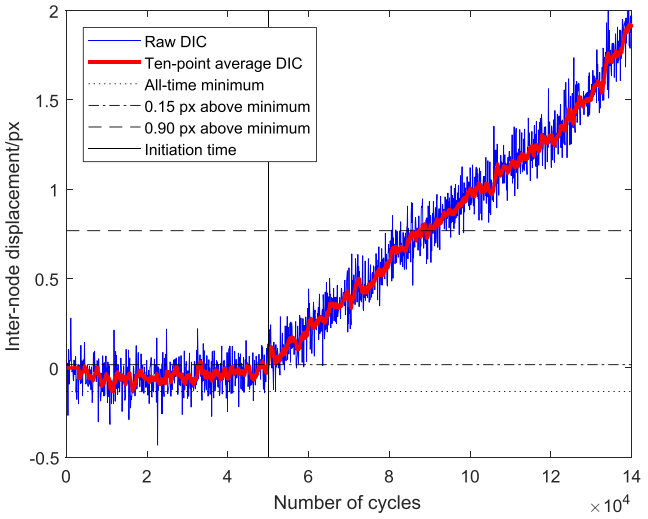

Fig. 7. Crack initiation detection criterion applied on a node pair in y direction. Initiation was said to happen at the last time the displacement curve crossed the line for 0.15 px above the all-time minimum, corresponding to a displacement of 2 μm.

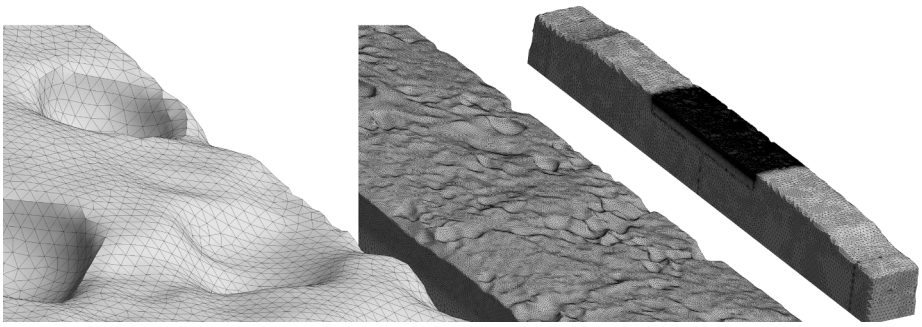

Fig. 8. Different zooms on the finite element surface mesh used for the midsection of specimen 3.

grade steel from [21] was used. Stress amplitudes in the y direction of the specimens, S_{ya}, were exported and used for the fatigue analysis.

2.3. Censoring data for multiple initiation events

On a corroded surface, corrosion pits and other stress irregularities act as stress raisers that are often highly local. Since a crack growing from a pit into a sharply decreasing stress field may need time to develop, time is left for secondary cracks to initiate from other areas with less severe stress states. Since the DIC technique can detect initiation and growth of secondary cracks, this can provide statistical insights when coupled with the stress results from FEA. Since the surface stresses will be altered in a region surrounding the growing cracks, the initiation events should be censored if they are significantly influenced by neighboring cracks.

A "stress sensitivity analysis" from a growing crack was performed, to see how the stress field compared to that of a crack-free specimen. As a worst-case example, a quarter-circular corner crack was placed in the x-z plane of a specimen with smooth surfaces loaded in three-point bending, see Fig. 9. Fig. 10 shows how S_y change at distances from the center of the crack. As an example, the presence of a 1-mm crack is marked by dotted lines. They show that at distances greater than 1.9 and 3.6 mm from the crack center, S_y on path x and y, respectively, was less than 5% affected by the crack.

Based on the results in Fig. 10, an algorithm for classifying crack initiation events as "independent" was implemented in MATLAB: The crack development log from DIC was replayed cycle by cycle. The first

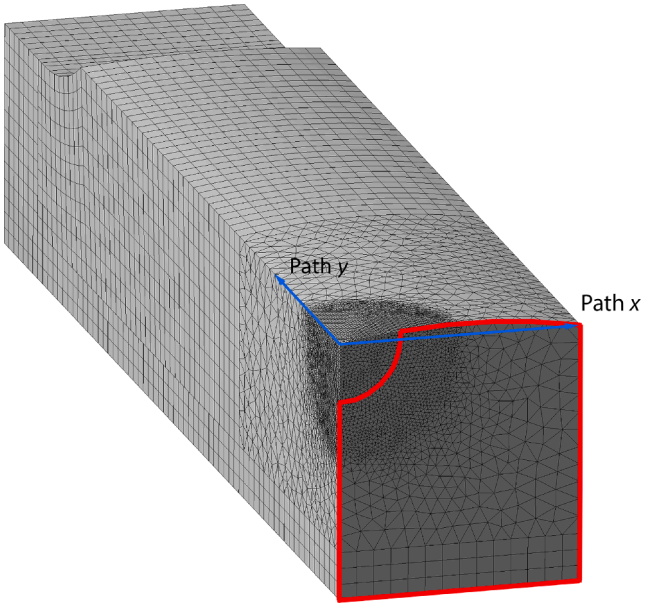

Fig. 9. FEA model for stress field sensitivity analysis for cracks of different sizes. The region enclosed in red is fixed in y direction at the x-z plane. Paths x and y are marked for outputting stresses.

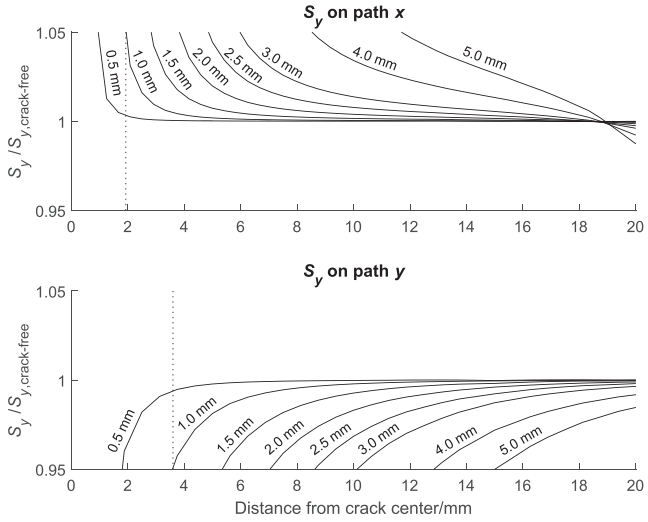

Fig. 10. S_y in a corner-cracked specimen with crack lengths 0.5 to 5 mm compared to a crack-free specimen. Stresses on paths x and y from Fig. 9 are shown. The dotted lines mark the distance from the crack center where a 1 mm crack causes 5% change in the stress field.

initiation was identified as stated earlier. As load cycling progressed, and further growth of the crack was registered by DIC, a 5% change in stress around the crack was said to invalidate the original FEA stress result. Only subsequent initiations *outside* of the region affected by the crack stresses were registered as new, independent initiations. As more cracks initiated, more regions of FEA stress were invalidated.

These conditions were enforced by virtually lining up rectangular areas around initiation sites, as cracks grew from them, and censoring any initiations happening within the rectangles. The rectangle sides had half lengths corresponding to crossings of the 5% lines in Fig. 10. Since Fig. 10 is based on a worst-case crack, this was thought to be a conservative approach. When the surface length of any crack in a specimen exceeded 3 mm, the effect on the original FEA stress field of a specimen was considered so extensive that the remaining stress field was invalidated.

2.4. Statistical treatment of results

The described algorithm returns data on initiation events on a specimen; however, it could also map regions that had survived without crack initiation at a given time. These data can be taken into account in the statistical treatment of the results. In the current work, the FEA stress amplitude fields for the midsection of each specimen were discretized into 0.1-by-0.1 mm, homogeneously stressed surface elements. Since it was known which elements experienced crack initiation and which did not, the best S-N curve fit to the data could be found using maximum likelihood regression. That is, an S-N curve was fitted to a few initiation events per specimen, as well as to the survival of every other 0.1-by-0.1

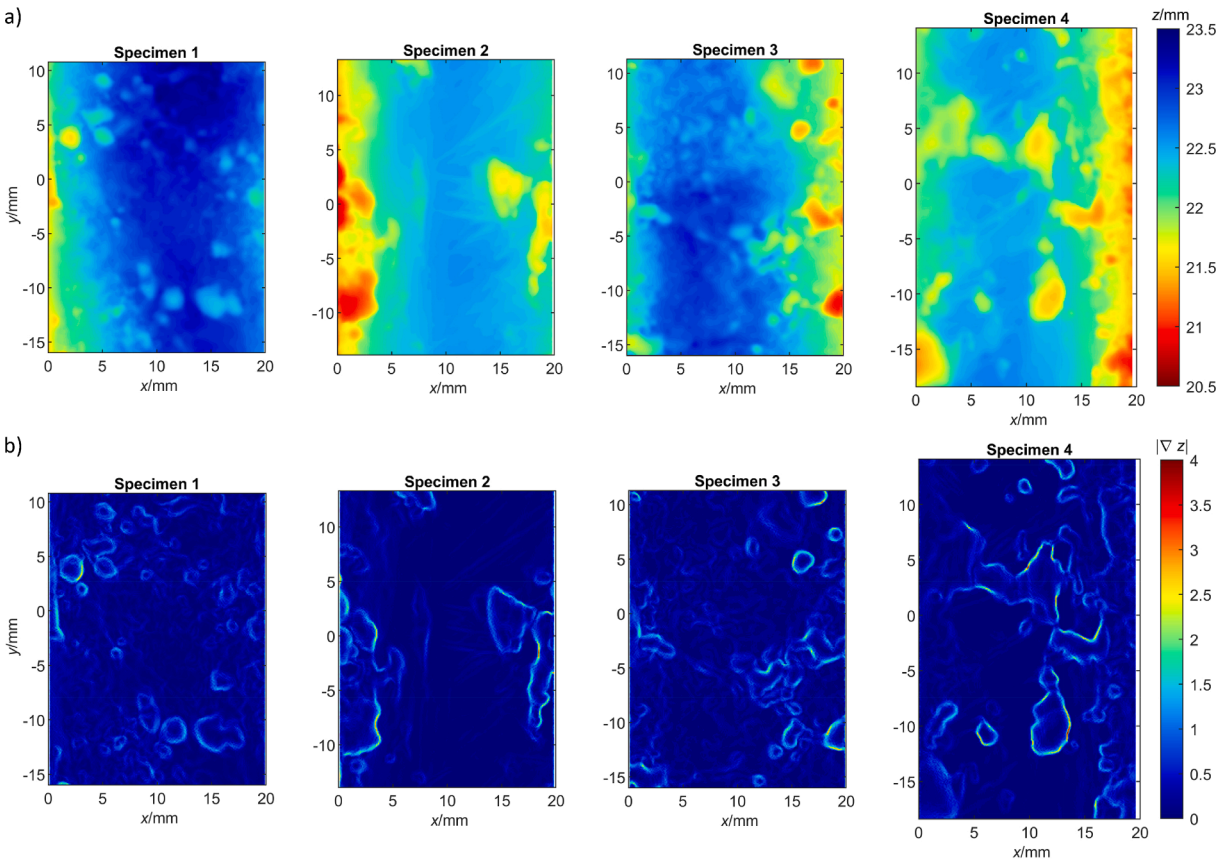

Fig. 11. a) Height profile and b) gradient plots of the midsection from every specimen.

mm surface element.

The curve fit was done by maximizing the *log-likelihood* function[28],

$$\mathscr{L} = \sum_{i=1}^{k} [\delta_i \log p_i + (1 - \delta_i) \log P_s] \tag{1}$$

for all k surface elements. Here, δ is an indicator function, which takes the value 1 if there is crack initiation in an element, and 0 if there is not. If the initiation lifetime is assumed to be Weibull distributed, then the probability density function for initiation, p_i, and the cumulative distribution function for survival, P_s, of a surface element, is given by[29]

$$\begin{aligned} p_i &= \frac{\ln 2 \cdot \beta_N \left(\frac{n}{N}\right)^{\beta_N}}{n \cdot 2^{\left(\frac{n}{N}\right)^{\beta_N}}} \text{ and} \\ P_s &= 2^{-\left(\frac{n}{N}\right)^{\beta_N}}, \end{aligned} \tag{2}$$

where β_N is the Weibull shape parameter, a measure of initiation lifetime scatter. n is the number of cycles recorded for the surface element, and N is the median initiation lifetime, given by the *S-N* curve[6],

$$N = A S_{ya}^{b}, \tag{3}$$

where S_{ya} is the stress amplitude in the y direction. A and b are fitting constants, and $1/b$ states the slope of the *S-N* curve in a diagram with logarithmic axes.

3. Results

Height profile and gradient plots calculated from surface scans of the specimen midsections are shown in Fig. 11. Because of a limit in the maximum allowable number of nodes in the DIC software, only 27–32 mm length segments containing the biggest pits around the middle of the specimens were analyzed. The plots in Fig. 11 have been cropped to show only these areas. It can be seen from the height profiles that, because of the irregular nature of the corroded chain surface, the actual

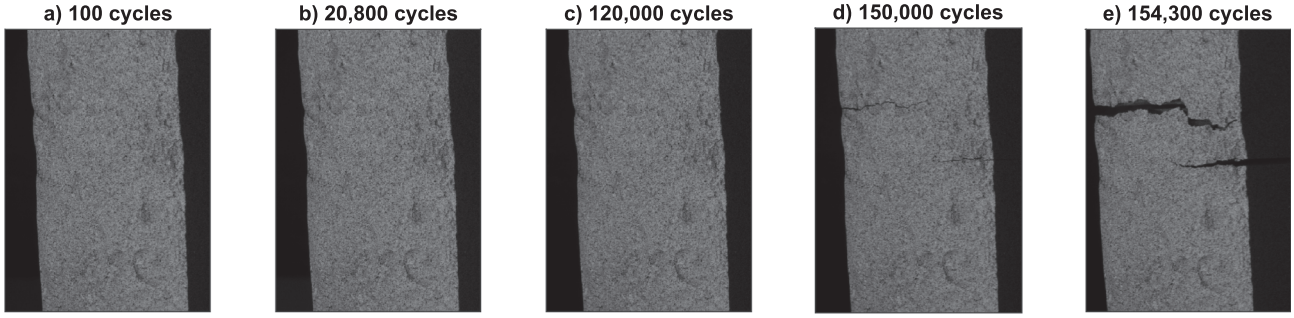

Fig. 12. Photographs of specimen 1 taken by the right camera a) at first frame, b) at 13%, c) 78% and d) 97% of the specimen lifetime and e) at the last frame before final fracture.

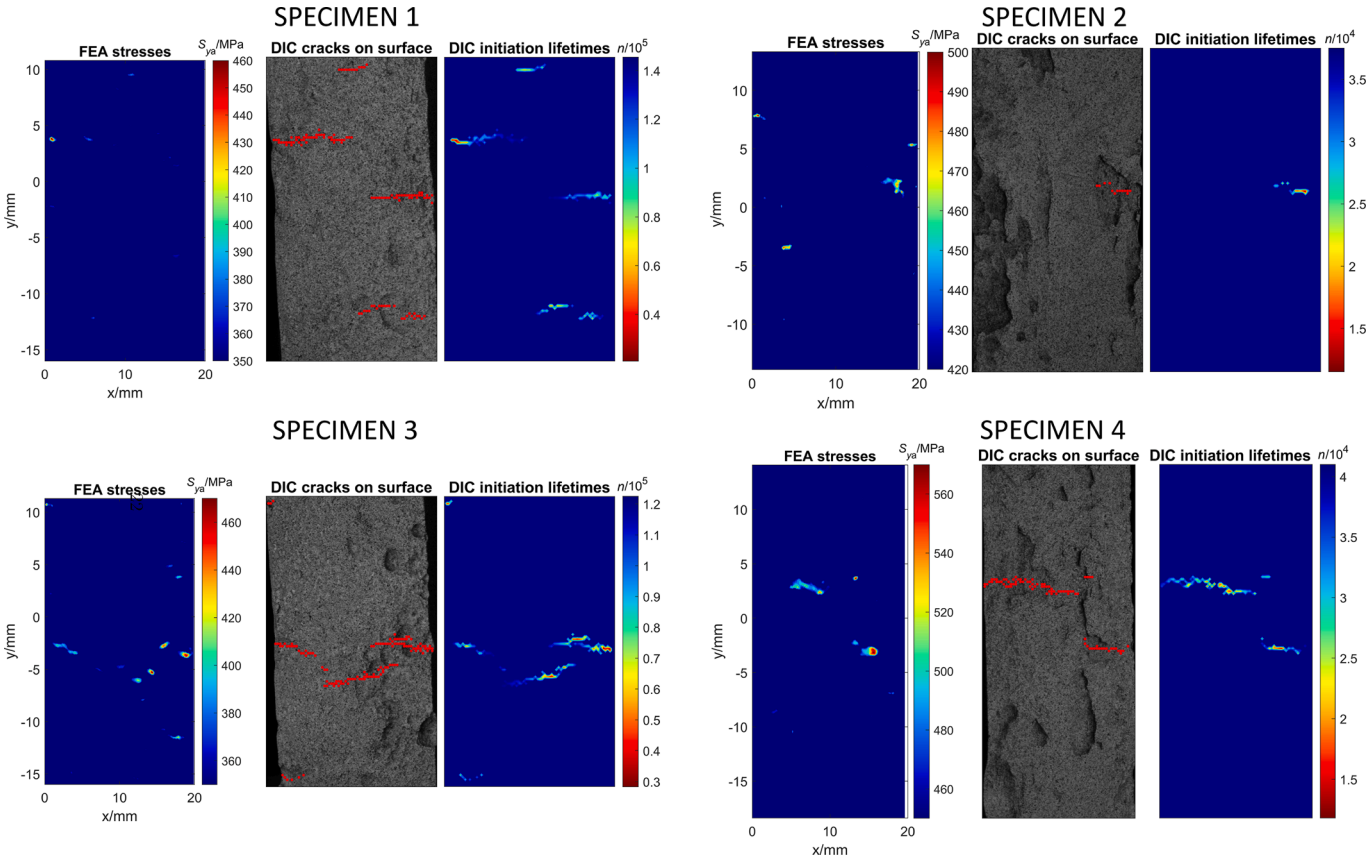

Fig. 13. Maps of stress amplitudes calculated with FEA (left) and crack initiation lifetimes measured with the crack initiation criterion on DIC results (right) for every specimen. The middle maps show crack development from DIC plotted on raw photographs of the specimen surfaces.

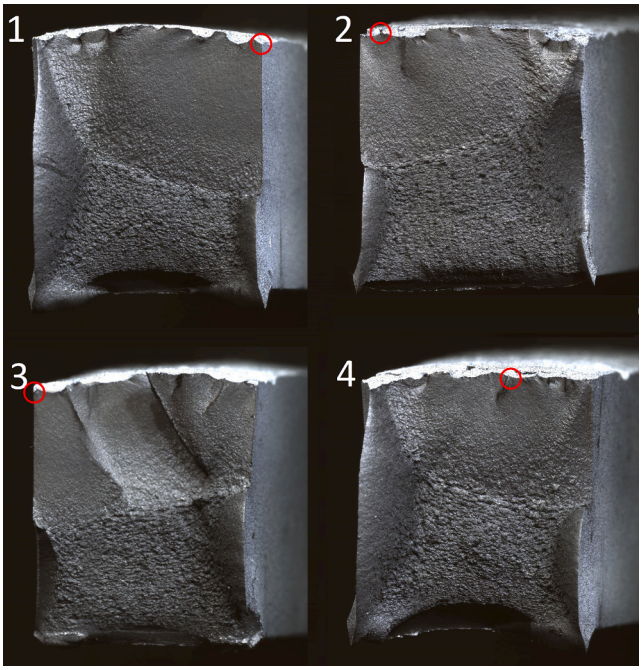

Fig. 14. Fracture surfaces of all specimens, viewed from positive y side. Red circles mark the earliest initiation sites for each surface.

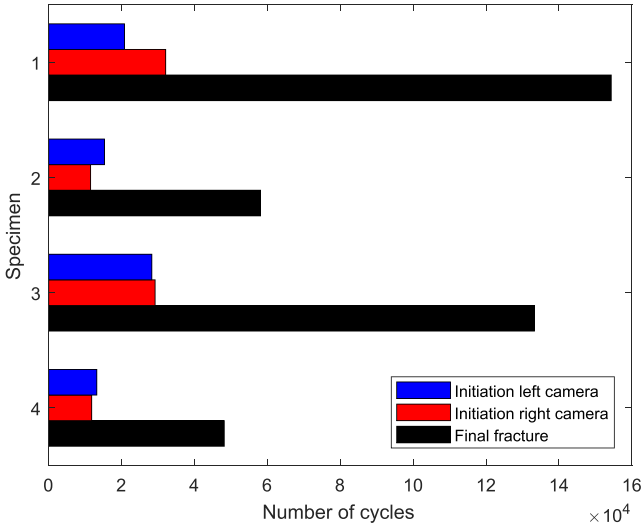

Fig. 15. Initiation and total lifetimes for all specimens.

maximum heights of the specimens varied between 22.6 and 23.5 mm. Specimen 2 and 4 seem to have a lower number of individual pits, but the pits have somewhat steeper walls than those in specimen 1 and 3, indicated by larger height gradients at the edges.

Fig. 12 shows examples of the raw photographs taken of the midsection of specimen 1 at different times for the purpose of DIC post-processing. To the naked eye, changes in the surface are barely visible even at frame c, at 78% of the specimen lifetime. In frame d, at 97% of the specimen lifetime, the crack that soon thereafter lead to final fracture, can be easily seen, along with one other crack.

The left sides of Fig. 13 show plane maps of stress amplitudes from FEA for all specimens. The color scales have been capped at the lower end to highlight the regions of relevant, high stresses. The right sides of Fig. 13 shows maps of initiating and growing cracks that were identified from DIC. The photographs of crack-free specimen surfaces are displayed in the middle figures, with red dots marking the locations where

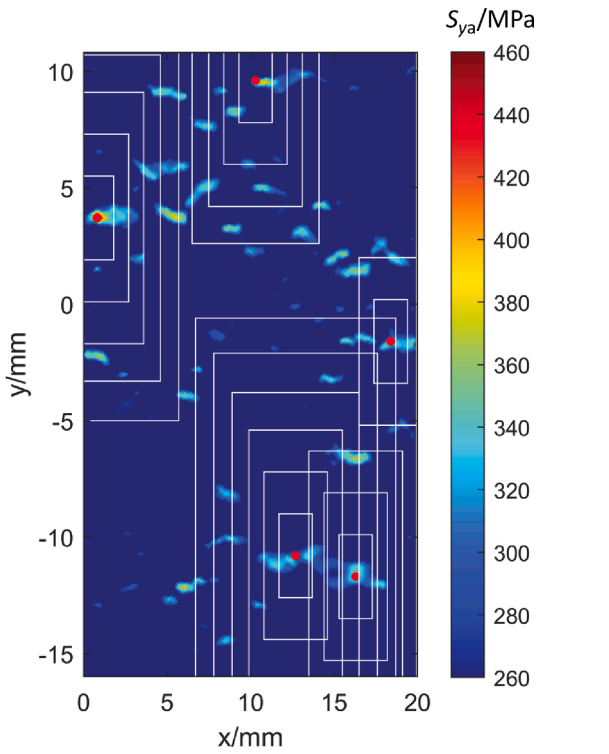

Fig. 16. Illustration of search algorithm for crack initiation applied to specimen 1. Red dots show crack initiation locations found by DIC, and the rectangles successively invalidates the FEA stress results in enclosing areas as cracks grow.

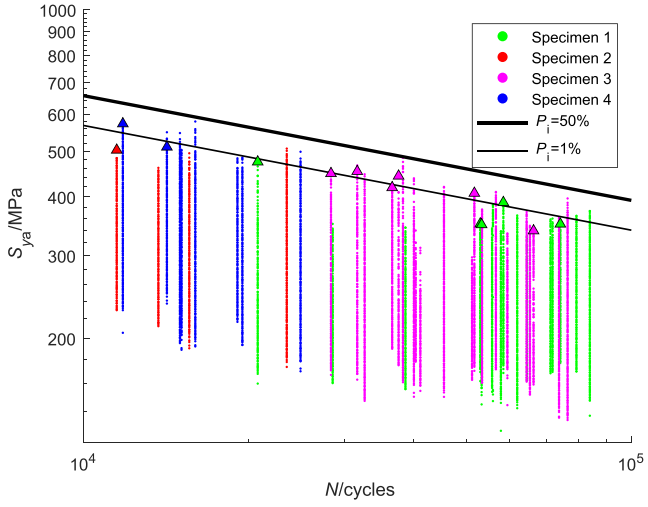

Fig. 17. An S-N curve for initiation in 0.1-by-0.1 mm element fitted to initiation and survival events from every specimen. The curve has a slope of $b = -4.49$ when taking the logarithms of the axes.

crack development occurred. Note that in the DIC maps, the cracks are plotted according to their location on the photographs, which might deviate slightly from locations of the corresponding stress concentrations in the plane coordinate systems of the FEA maps.

Fig. 13 shows that there is good correspondence between the calculated stresses and the initiation location of each crack. Several cracks were detected in all but specimen 2. When looking at Fig. 13, more cracks can be seen in the DIC plot for specimen 1 compared to Fig. 12. Moreover, the DIC criterion was shown to detect cracks at an early stage. As early as in frame b of Fig. 12, crack initiation was

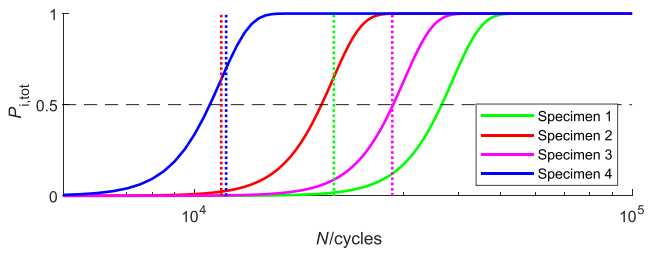

Fig. 18. Calculated probabilities of crack initiation for all specimens (solid lines), as well as recorded initiation lifetimes (dotted lines).

registered by DIC. No changes in the specimen surface were visible to the naked eye until much later.

As a crack grows and opens, a dark line becomes apparent on the photographs, as seen in Fig. 12. Eventually, the part of the DIC mesh interfering with the crack starts to break down and produce invalid displacement results. Therefore, this work was limited to detection of crack initiation and growth of small cracks. DIC measurements past the point of mesh breakdown were discarded. This is one reason why complete crack paths at final fracture are not shown on the crack development maps in Fig. 13. The time of mesh breakdown is stated by the maximum value on the color scale.

Another reason that full crack paths are not visible in Fig. 13, is that the initiation criterion works in retrospect. For crack initiation to be registered at a node pair, the inter-node displacement has to reach 0.90 px, even though the actual initiation time is registered earlier, at a time of only 0.15 px displacement. The result is that any node pair with a displacement between 0.15 and 0.90 px at the time of mesh breakdown does not show up on the crack development maps as initiated.

Macrographs of the final fractures of all specimens are shown in Fig. 14. Red circles mark the sites of the first initiations on the final crack surfaces. For the case of specimen 3 and 4, this was not the first initiation site for the specimen as a whole. In these specimens, secondary cracks outgrew the first crack that initiated. Since the crack development maps

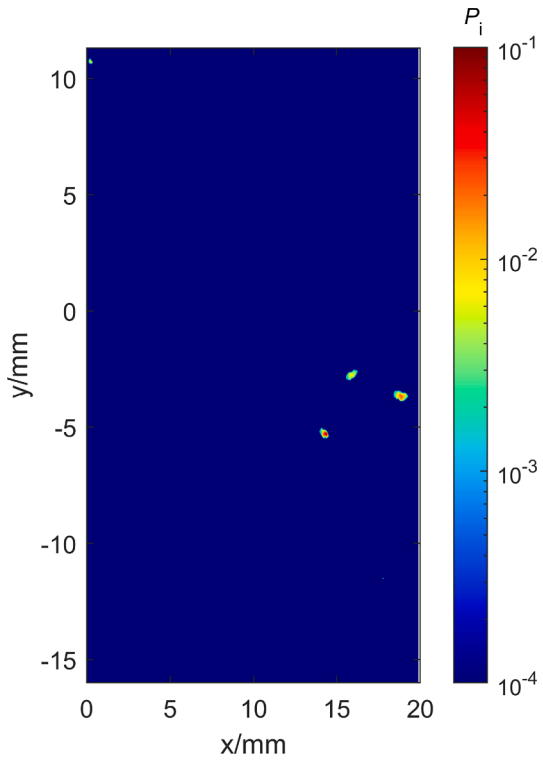

Fig. 20. Map of element crack initiation probability for the midsection of specimen 3 at the moment of measured initiation.

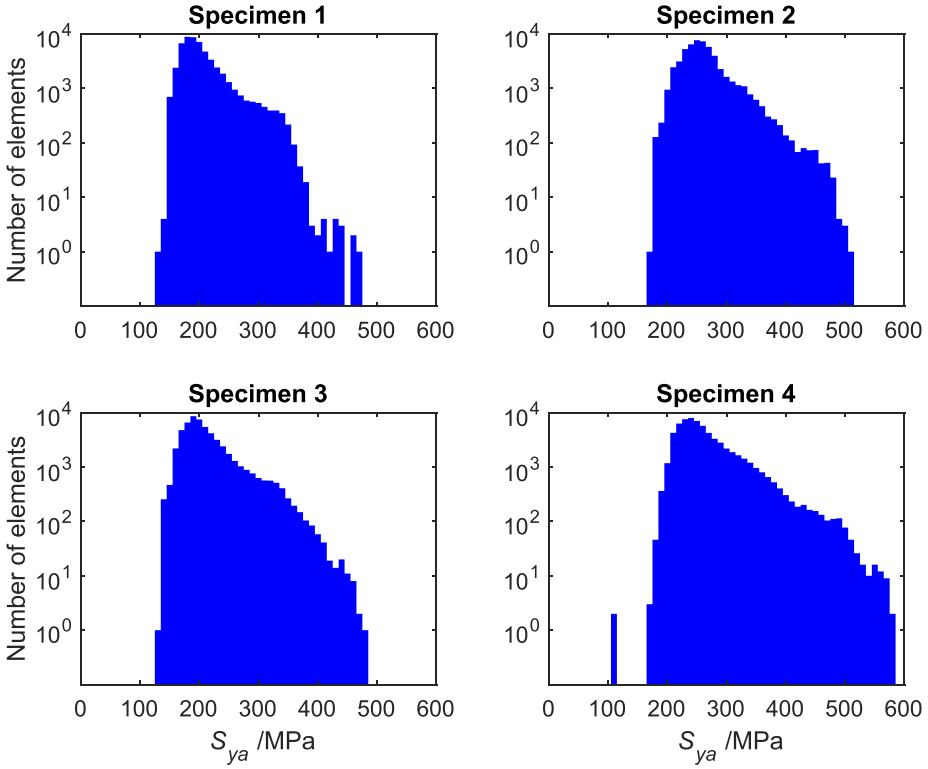

Fig. 19. S_{ya} distributions for all specimens, discretized into 10-MPa levels.

in Fig. 13 show cracks at a much earlier stage, it is difficult to correlate them completely to the appearance of the final fracture surfaces. However, Fig. 14 still provides some validation of the initiation location and early crack development measured by DIC.

Fig. 15 shows the total lifetimes for all specimens, registered at the final, unstable fracture. The earliest initiation lifetimes recorded by each camera is also shown. The deviations in the initiation lifetime could be due to differences in depth of field and field of view for the two cameras, or due to noise in the DIC results. Fig. 13 displays results from the camera showing the earliest initiation for each specimen. In order to produce conservative initiation lifetime results, that same camera was used for further results processing for the specimen.

It can be seen from Fig. 15 that crack growth dominates the fatigue lives at the current load levels, accounting for 76–87% of the lifetime of the specimens.

The algorithm for logging initiation events is illustrated in Fig. 16. The contour plot shows FEA stresses, and the red dots mark all initiation sites. As cycling progresses, the rectangles lined up in white encloses progressively larger regions of the specimen surface.

Data about initiation and survival of surface elements for all specimens has been plotted in an *S-N* diagram in Fig. 17. Dots mark survived elements, and triangles mark initiations. It should be noted that a total of fourteen independent initiation events could be plotted from the four specimens, i.e. ten more than from an ordinary fatigue test. Every region on a specimen being enclosed by a rectangle is shown by a vertical line of data points. For each specimen, the data points are spread out over a large portion of total lifetime. Thus, for components where the first crack initiation occurs early, the method provides a good basis for *S-N* curve fitting even for single-load-level test programs. An *S-N* curve, marked by black lines, was fitted to the results using maximum likelihood regression. The curve represents the probability of a crack initiating in a 0.1-by-0.1 mm element at a given time.

Solid lines in Fig. 18 shows the total cumulative distribution function of first initiation for every specimen, found by multiplication of element survival probabilities. The dotted lines represent the earliest recorded initiations. While cracks initiate in all specimens within the limits of the scatter, it happens at very low probabilities for specimen 1 and 2. The explanation lies in Fig. 17: Even though the *S-N* curve is based on data points from all specimens, specimen 1 and 2 have few surface elements that are stressed to levels of high initiation probability *at the moment of first initiation*. This just shows that there are variations in fatigue properties between the specimens, or between locations on them, that cannot be identified by stress calculations of the current scale.

Fig. 19 shows the number of surface elements exposed to each stress amplitude level for all specimens. As expected, it can be seen in Fig. 18 that it is the highest stress amplitudes, and the size of the area they cover, that controls the lifetime ranking of the specimens. Specimens 3 and 4 have more severe stress states than the correspondingly loaded specimens 1 and 2.

Finally, element crack initiation probabilities can be plotted as in Fig. 20. Although the appearance might not be much different from that of a stress amplitude map, it provides a properly scaled, graphical representation in the initiation probability across a specimen surface. It can be developed into a tool for quantitatively comparing the severity of corrosion pits of different shapes.

4. Discussion

Stresses in corrosion pits were calculated with FEA. Even though the mesh was not fine enough to capture stresses induced by microscopic surface features and roughness from corrosion, the calculated surface stresses showed a good correlation with initiation lifetimes, and an *S-N* curve with low scatter was produced. This may indicate that the detrimental effect on initiation life of any smaller-scale features is largely even across the surface. Thus, even though the macroscopic appearance of corrosion has been shown to vary significantly between mooring chain links[2], the constructed *S-N* curve might still be valid if stresses are calculated from FEA with the current mesh resolution. However, this follows an assumption that microscopic surface damage from general corrosion is equal for all levels of macroscopic damage, which is debatable. To further reduce scatter in lifetime predictions, microscopic surface profiles could be included in the FEA[30]. Taking into account sub-surface stress distributions could also reduce scatter[31].

A geometric feature that is present in the specimens, but not in a chain link, is the sidewalls. The lack of surrounding material near the edges of the corroded surface lowers constraint, facilitating crack initiation. This effect on the stress fields is well represented by the FEA and does not lead to any discrepancies between recorded lifetimes and calculated initiations stresses. However, cutting by EDM has been shown to introduce detrimental residual stresses, defects and metallurgical transformations[32], and milling is known to introduce shallow residual stresses that can affect fatigue lifetime both positively and negatively [33]. Since these effects are not accounted for in the FEA, they can be a source of scatter in the *S-N* curve. From Fig. 13 it can be seen that some cracks initiated from the edges of specimen 1 and 3. Even though most of these initiated from areas with high calculated stresses, the influence from machining stresses cannot be ruled out completely.

In the current tests, large fractions of the specimen lifetimes were found to be spent on crack growth. This indicates that the crack growth phase should be the main one to focus on for the purpose of lifetime prediction at the current stress levels. In full-size chain links, there might be larger surface regions of high stress than in the specimens. This would increase the probability of early crack initiation. Moreover, the cross sections are larger, so cracks have to grow longer before final fracture. Thus, the lifetime fraction of crack growth for a chain link might be even larger than what was registered for the specimens. However, if the chains are loaded to lower stresses, the situation may be another. Future small-scale tests should be run at load levels that give surface stresses corresponding to relevant full-scale tests of mooring chain segments.

Moreover, the current specimens were not tested in seawater. Even though the effects of the corrosive medium on crack initiation and growth lifetimes are less in laboratory fatigue tests of chain segments than in service, it should not be overlooked.

The effect of mean stresses was not considered here. Mean stresses are likely to affect the processes of crack initiation and growth from a corroded surface differently. Changing the mean stress might thus alter the time fractions of initiation and growth. In the current work, mean stress relaxation occurred in highly stressed areas because of yielding during the initial upload. In the most highly stressed point on specimen 4, R was reduced from 0.2 to -0.2. However, stress-raising, microscopic surface features might have caused the actual mean stress relaxation to be even more pronounced than calculated by FEA. In mooring chains, residual stresses from production have been identified as compressive in some critical crack initiation locations[22]. When superposing these to fatigue loading of the chains, R values may effectively be lowered. By designing a fatigue test program with more varying mean loads, the techniques described in the current work can be applied to investigate the effects on fatigue initiation life of corroded specimens.

DIC showed to be sensitive enough for crack detection, even when based on photographs of a highly irregular surface captured from an angle. High node coordinate resolution and accuracy is achievable and can likely be increased by rerunning the analyses using meshes where elements do not span the currently identified crack paths[26]. However, the crack initiation criterion could be made more robust, and alternative criteria could be evaluated. Moreover, better routines for transforming coordinates between DIC and FEA results should be developed, since manual linking is time consuming and vulnerable to human error. Any routine would benefit from more ideal camera placement.

Locations of the initiation sites were manually measured from the DIC maps in Fig. 13. This procedure may be prone to manual measuring errors and inaccuracies caused by the limited resolution of the DIC mesh. Therefore, based on an estimate of manual measuring accuracy, a

tolerance was included on initiation site location: When counting an initiation event, the highest stress within a 0.6 mm distance from the located initiation site was considered to be the initiation stress. However, this definition leads to a bias in the results, when concluding that the highest FEA stress is controlling crack initiation. The problem would be lessened if tolerances in initiation site localization could be lowered. This would be possible if using a more accurate coordinate linking technique and a finer DIC mesh.

Crack initiation in smooth specimens begins with cyclic slip within a single grain[6]. Since the element size in the DIC meshes in the current work is considerably larger than the grain size of the steel, it is unlikely that any intra-grain displacements would be picked up by the measurements. Additionally, the paint on the specimen surfaces likely acts to soften the most local discontinuities in the displacement field that is visible to the cameras. This means that the displacement that is measured as initiation at a node pair in the current work presumably comes from the strain field in front of, or opening of, a crack that is already spanning multiple grains. Considering that a DIC element measures 0.3 mm in the x direction, a crack with a strain field of that same width could go unnoticed. Since the initiation criterion works in retrospect, it would be difficult to stop a fatigue test at the time of initiation in order to examine the crack appearance.

The idea of taking the stress distribution across the whole specimen surface into account when calculating the probability of failure is not new. Discretization of the surface into homogeneously stressed elements represents a primitive application of the weakest link method[34]. A more advanced stress integration scheme could improve accuracy.

For future work, it is planned to apply the constructed crack initiation *S-N* curve to results from full-scale fatigue tests of chain links. If the total life of chain links could be predicted by combining results from the constructed *S-N* curve and those of an appropriate crack growth model, this would provide validation of the results obtained in the current work.

5. Conclusions

Specimens cut from corroded mooring chain links were fatigued in three-point bending, and the DIC technique was used to detect crack initiation locations. The initiation stresses were calculated by FEA. An algorithm for defining independent crack initiation events was implemented, and the results were used to construct a crack initiation *S-N* curve for corroded surfaces of mooring chains.

It was shown that DIC provides suitable coordinate data for detecting initiation and growth of multiple cracks on a corroded surface. When more crack initiation data is available per specimen, the number of specimens needed to develop a statistically sound results database is reduced, lowering testing costs.

For the current load levels, it was found that cracks initiated from the corroded surface within 13–24% of the total specimen lifetime. The fact that the majority of the specimen lifetimes were spent in crack growth, suggests that the primary focus should be on this phase for fatigue lifetime predictions of mooring chains. However, the current test program was limited in terms of stress levels, and a single stress ratio of $R = 0.2$ was used. Other stress states in mooring chains might yield other divisions of lifetimes in full-scale tests.

Declaration of Competing Interest

The authors declare that they have no known competing financial interests or personal relationships that could have appeared to influence the work reported in this paper.

Acknowledgments

The authors would like to acknowledge Christian Frugone (NTNU), for his extensive efforts in setting up the fatigue rig systems. Acknowledgment also goes to Trond Auestad, Egil Fagerholt and Per J. Haagensen (NTNU), for discussions on the DIC monitoring and fatigue test setup. The authors are grateful for financial support for the work received through the project KPN Lifemoor (RCN contract No: 280705).

References

[1] Gabrielsen Ø, Liengen T, Molid S. Microbiologically influenced corrosion on seabed chain in the north sea, in. In: Proceedings of the ASME 2018 37th International Conference on Ocean, Offshore and Arctic Engineering. ASME; 2018. https://doi.org/10.1115/OMAE2018-77460.

[2] K. Ma, Ø. Gabrielsen, Z. Li, D. Baker, A. Yao, P. Vargas, M. Luo, A. Izadparast, A. Arredondo, L. Zhu, N. Sverdlova, I.S. Høgsæt, Fatigue tests on corroded mooring chains retrieved from various fields in offshore west africa and the north sea, in: Proceedings of the ASME 2019 38th International Conference on Ocean, Offshore and Arctic Engineering [35]. doi: 10.1115/OMAE2019-95618.

[3] Fernández J, Storesund W, Navas J. Fatigue performance of grade r4 and r5 mooring chains in seawater, in. In: Proceedings of the ASME 2014 33rd International Conference on Ocean, Offshore and Arctic Engineering. ASME; 2014. https://doi.org/10.1115/OMAE2014-23491.

[4] Ø. Gabrielsen, K. Larsen, O. Dalane, H.B. Lie, S. Reinholdtsen, Mean load impact on mooring chain fatigue capacity: Lessons learned from full scale fatigue testing of used chains, in: Proceedings of the ASME 2019 38th International Conference on Ocean, Offshore and Arctic Engineering omae19. doi: 10.1115/OMAE2019-95083.

[5] Thorpe TW, Scott PM, Rance A, Silvester D. Corrosion fatigue of BS 4360:50D structural steel in seawater. Int. J. Fatigue 1983;5(3):123–33. https://doi.org/10.1016/0142-1123(83)90025-7. https://www.sciencedirect.com/science/article/pii/0142112383900257.

[6] Schijve J. Fatigue of Structures and Materials. 2nd Edition,. Netherlands: Springer; 2009. https://doi.org/10.1007/978-1-4020-6808-9.

[7] Gkatzogiannis S, Weinert J, Engelhardt I, Knoedel P, Ummenhofer T. Correlation of laboratory and real marine corrosion for the investigation of corrosion fatigue behaviour of steel components. Int. J. Fatigue 2019;126:90–102. https://doi.org/10.1016/j.ijfatigue.2019.04.041. http://www.sciencedirect.com/science/article/pii/S014211231930163X.

[8] Igwemezie V, Mehmanparast A. Waveform and frequency effects on corrosion-fatigue crack growth behaviour in modern marine steels. Int. J. Fatigue 2020;134:105484. https://doi.org/10.1016/j.ijfatigue.2020.105484. http://www.sciencedirect.com/science/article/pii/S0142112320300153.

[9] Turnbull A. Characterising the early stages of crack development in environment-assisted cracking. Corros. Eng., Sci. Technol. 2017;52(7):533–40. https://doi.org/10.1080/1478422X.2017.1348761.

[10] Evans C, Leiva-Garcia R, Akid R. Strain evolution around corrosion pits under fatigue loading. Theoret. Appl. Fract. Mech. 2018;95:253–60. https://doi.org/10.1016/j.tafmec.2018.02.015. http://www.sciencedirect.com/science/article/pii/S0167844218300387.

[11] Nicolas A, Co NEC, Burns JT, Sangid MD. Predicting fatigue crack initiation from coupled microstructure and corrosion morphology effects. Eng. Fract. Mech. 2019;220:106661. https://doi.org/10.1016/j.engfracmech.2019.106661. http://www.sciencedirect.com/science/article/pii/S0013794419303005.

[12] Liu L, Hou N, Ding N, Guo W. Interacting Effects of Internal Defects and Corrosion Pits on the Stress Concentration of Hourglass-Shaped Specimens. J. Fail. Anal. Prev. 2019;19(4):967–75. https://doi.org/10.1007/s11668-019-00682-2.

[13] Chen J, Diao B, He J, Pang S, Guan X. Equivalent surface defect model for fatigue life prediction of steel reinforcing bars with pitting corrosion. Int. J. Fatigue 2018;110:153–61. https://doi.org/10.1016/j.ijfatigue.2018.01.019. http://www.sciencedirect.com/science/article/pii/S0142112318300239.

[14] Zhao T, Liu Z, Du C, Liu C, Xu X, Li X. Modeling for corrosion fatigue crack initiation life based on corrosion kinetics and equivalent initial flaw size theory. Corros. Sci. 2018;142:277–83. https://doi.org/10.1016/j.corsci.2018.07.031. http://www.sciencedirect.com/science/article/pii/S0010938X18305687.

[15] M.D. McMurtrey, D.E. Mills, J.T. Burns, The effect of pit size and density on the fatigue behaviour of a pre-corroded martensitic stainless steel, Fatigue & Fracture of Engineering Materials & Structures 42 (1) (2019) 3–18, _eprint: https://onlinelibrary.wiley.com/doi/pdf/10.1111/ffe.12860. doi:10.1111/ffe.12860. https://onlinelibrary.wiley.com/doi/abs/10.1111/ffe.12860.

[16] E. Jones, M.E. Iadicola, A Good Practices Guide for Digital Image Correlation, 2018. doi:10.32720/idics/gpg.ed1.

[17] Mathieu F, Hild F, Roux S. Identification of a crack propagation law by digital image correlation. Int. J. Fatigue 2012;36(1):146–54. https://doi.org/10.1016/j.ijfatigue.2011.08.004. https://www.sciencedirect.com/science/article/pii/S0142112311002027.

[18] Zhu M-L, Lu Y-W, Lupton C, Tong J. In situ near-tip normal strain evolution of a growing fatigue crack. Fatigue & Fracture of Engineering Materials & Structures 2016;39(8):950–5. https://doi.org/10.1111/ffe.12391. https://onlinelibrary.wiley.com/doi/abs/10.1111/ffe.12391.

[19] J.D. Carroll, W. Abuzaid, J. Lambros, H. Sehitoglu, High resolution digital image correlation measurements of strain accumulation in fatigue crack growth, International Journal of Fatigue 57 (2013) 140–150, fatigue and Microstructure: A special issue on recent advances. doi: 10.1016/j.ijfatigue.2012.06.010. https://www.sciencedirect.com/science/article/pii/S0142112312002113.

[20] Rupil J, Roux S, Hild F, Vincent L. Fatigue microcrack detection with digital image correlation. The Journal of Strain Analysis for Engineering Design 2011;46(6):492–509. https://doi.org/10.1177/0309324711402764.

[21] Zarandi EP, Skallerud BH. Cyclic behavior and strain energy-based fatigue damage analysis of mooring chains high strength steel. Marine Structures 2020;70:102703. https://doi.org/10.1016/j.marstruc.2019.102703. http://www.sciencedirect.com/science/article/pii/S0951833919304186.

[22] Zarandi EP, Skallerud BH. Experimental and numerical study of mooring chain residual stresses and implications for fatigue life. Int. J. Fatigue 2020;135:105530. https://doi.org/10.1016/j.ijfatigue.2020.105530. https://www.sciencedirect.com/science/article/pii/S014211232030061X.

[23] Martinez Perez I, Constantinescu A, Bastid P, Zhang Y-H, Venugopal V. Computational fatigue assessment of mooring chains under tension loading. Engineering Failure Analysis 106 2019:104043. https://doi.org/10.1016/j.engfailanal.2019.06.073. https://www.sciencedirect.com/science/article/pii/S1350630718310914.

[24] ASTM International, West Conshohocken, PA, G1–03(2017) e1 Standard Practice for Preparing, Cleaning, and Evaluating Corrosion Test Specimens (2017). doi: 10.1520/G0001-03R17E01.

[25] Gabrielsen Ø, Larsen K, Reinholdtsen S-A. Fatigue testing of used mooring chain, in. In: Proceedings of the ASME 2017 36th International Conference on Ocean, Offshore and Arctic Engineering. ASME; 2017. https://doi.org/10.1115/OMAE2017-61382.

[26] Fagerholt E, Børvik T, Hopperstad O. Measuring discontinuous displacement fields in cracked specimens using digital image correlation with mesh adaptation and crack-path optimization. Opt. Lasers Eng. 2013;51(3):299–310. https://doi.org/10.1016/j.optlaseng.2012.09.010. https://www.sciencedirect.com/science/article/pii/S0143816612002801.

[27] S.S. Gorthi, P. Rastogi, Fringe projection techniques: Whither we are?, Optics and Lasers in Engineering 48 (2) (2010) 133–140, fringe Projection Techniques. doi: 10.1016/j.optlaseng.2009.09.001. https://www.sciencedirect.com/science/article/pii/S0143816609002164.

[28] Pollak RD, Palazotto AN. A comparison of maximum likelihood models for fatigue strength characterization in materials exhibiting a fatigue limit. Probab. Eng. Mech. 2009;24(2):236–41. https://doi.org/10.1016/j.probengmech.2008.06.006. http://www.sciencedirect.com/science/article/pii/S026689200800057X.

[29] Wormsen A, Härkegård G. Weibull fatigue analysis of notched components under constant and variable amplitude loading. In: Proceedings of the 9th International Fatigue Congress 2006. Elsevier; 2006.

[30] Skallerud B, Ås SK, Ottosen NS. A gradient-based multiaxial criterion for fatigue crack initiation prediction in components with surface roughness. Int. J. Fatigue 2018;117:384–95. https://doi.org/10.1016/j.ijfatigue.2018.08.020. https://www.sciencedirect.com/science/article/pii/S0142112318303943.

[31] Härkegård G, Halleraker G. Assessment of methods for prediction of notch and size effects at the fatigue limit based on test data by böhm and magin. Int. J. Fatigue 2010;32(10):1701–9. https://doi.org/10.1016/j.ijfatigue.2010.03.011. https://www.sciencedirect.com/science/article/pii/S0142112310000770.

[32] Ghanem F, Sidhom H, Braham C, Fitzpatrick ME. Effect of near-surface residual stress and microstructure modification from machining on the fatigue endurance of a tool steel. J. Mater. Eng. Perform. 2002;11(6):631–9. https://doi.org/10.1361/105994902770343629. https://doi.org/10.1361/105994902770343629.

[33] H. Sasahara, The effect on fatigue life of residual stress and surface hardness resulting from different cutting conditions of 0.45%c steel, International Journal of Machine Tools and Manufacture 45 (2) (2005) 131–136. doi: 10.1016/j.ijmachtools.2004.08.002. https://www.sciencedirect.com/science/article/pii/S0890695504001853.

[34] Wormsen A, Sjödin B, Härkegård G, Fjeldstad A. Non-local stress approach for fatigue assessment based on weakest-link theory and statistics of extremes. Fatigue & Fracture of Engineering Materials & Structures 2007;30(12):1214–27. https://doi.org/10.1111/j.1460-2695.2007.01190.x.

[35] Proceedings of the ASME 2019 38th International Conference on Ocean, Offshore and Arctic Engineering, Vol. 3, ASME, 2019.